Strain-rate based arclength model for nonlinear microscale analysis of unidirectional composites under off-axis loading

Kovacevic, Dragan; van der Meer, Frans P.

DOI
10.1016/j.ijsolstr.2022.111697

Publication date
2022

Document Version
Final published version

Published in
International Journal of Solids and Structures

International Journal of Solids and Structures 250 (2022) 111697

Contents lists available at ScienceDirect

International Journal of Solids and Structures

journal homepage: www.elsevier.com/locate/ijsolstr

Strain-rate based arclength model for nonlinear microscale analysis of unidirectional composites under off-axis loading

Dragan Kovačević [a,b,*], Frans P. van der Meer [a]

[a] Delft University of Technology, Faculty of Civil Engineering and Geosciences, PO Box 5048, 2600 GA Delft, The Netherlands
[b] Dutch Polymer Institute (DPI), PO Box 902, 5600 AX, Eindhoven, The Netherlands

ARTICLE INFO

Dataset link: https://doi.org/10.4121/17166974.v1

Keywords:
Unidirectional composites
Strain-rate
Arclength method
Material nonlinearity
Geometric nonlinearity

ABSTRACT

In this paper, a micromechanical framework for modeling the rate-dependent response of unidirectional composites subjected to off-axis loading is introduced. The model is intended for a thin slice representative volume element that is oriented perpendicular to the reinforcement of the composite material. The testing conditions from a uniaxial off-axis test are achieved by a dedicated strain-rate based arclength formulation. The constraint equation of the arclength model is constructed such that the deformation state of the micromodel, as imposed in its local coordinate system, corresponds to the strain-rate applied on the material in global frame of reference. The kinematic description allows for finite strains in the material, meaning that the micromodel changes orientation during the deformation process. This geometric nonlinear effect is also included in the evaluation of external loading, ensuring that the external forces are equivalent to the applied off-axis stress in global coordinate system. Several examples are considered in order to show that the model resolves rate-dependency of the material, accounts for different off-axis loading, and captures finite strains exactly. Additionally, a small strain version of the model is derived from the general nonlinear framework. Results obtained with this simplified approach are compared to results of the large deformation framework.

1. Introduction

Continuous fiber reinforced composites are used in many load-carrying applications where structural reliability is of great importance. The ability to accurately predict the mechanical response of the material for different loading scenarios is essential in the optimal process of design and maintenance of those structures. In last decades the concept of the Representative Volume Element (RVE) has been used frequently to study the mechanics of heterogeneous materials on a scale of observation finer than the macroscopic scale. Several features of composite materials have been investigated through such microscale simulations. Melro et al. (2012) analyzed elastic properties of composites that differ from the properties of the individual constituents. Van der Meer (2016) compared the behavior of a homogenized orthotropic plasticity model for fiber reinforced composites with that of an RVE with plastic matrix and elastic fibers. Totry et al. (2008) calculated the strength of a composite lamina for different loading scenarios. Rocha et al. (2017) studied hygrothermal aging in laminated composites in a multiscale FE^2 framework. The in-situ effect in polymer composite laminates has been investigated by Arteiro et al. (2014). Naya et al. (2017) included environmental conditions, such as temperature and humidity, in predicting stiffness and strength properties of one ply. In a multiscale approach, Govaert et al. (2001) modeled the rate-dependent off-axis strength of unidirectional (UD) laminates.

Even though many features of UD composites can be studied on two-dimensional (2D) RVE, modeling of stress states that arise in off-axis testing requires formulation in 3D space because of the presence of stress in fiber direction and longitudinal shear stress. The aim of this work is to develop a micromechanical framework that accommodates geometric and material nonlinear analysis of UD composites exposed to uniaxial loading at a predefined strain-rate, with an arbitrary orientation of the reinforcement with respect to the loading direction, i.e., different off-axis angles. The framework is designed for the RVE of a thin slice of fiber reinforced composite material that is oriented perpendicular to the direction of the reinforcement. By using a thin slice, excessive computational costs that would be associated with a full 3D RVE with geometric representation of the off-axis fibers are avoided. The challenge addressed in this work is to satisfy the requirement that the deformation and stress state of the RVE, in its local coordinate frame, are equivalent to the state of the lamina in the global coordinate system of the off-axis experiment. The exact solution to this problem demands control over the update in nodal displacements of the RVE, which determines the strain-rate in the global frame of reference. Also,

* Corresponding author at: Delft University of Technology, Faculty of Civil Engineering and Geosciences, PO Box 5048, 2600 GA Delft, The Netherlands.
E-mail addresses: d.kovacevic-1@tudelft.nl (D. Kovačević), f.p.vandermeer@tudelft.nl (F.P. van der Meer).

https://doi.org/10.1016/j.ijsolstr.2022.111697
Received 22 December 2021; Received in revised form 26 April 2022; Accepted 3 May 2022
Available online 11 May 2022

it requires control over the external load level on the RVE, which is related to the uniaxial stress state in the global frame. Because of the requirement to simultaneously control both the displacements and the load level in the analysis, an arclength control formulation is pursued.

Arclength control methods stem from the work of Wempner (1971) and Riks (1972). In order to solve the problem of snap-back or snap-through behavior that may arise in a structural analysis, Riks added an auxiliary equation with a path following constraint to the existing set of equations. This framework is versatile in the sense that an arbitrary constraint can be defined. Initially the constraint equation was mostly based on a proper geometrical combination of norms of the nodal displacements and load increment. It was realized by De Borst (1987) that the constraint equation which includes all nodal degrees of freedom cannot be successfully applied to strain-softening problems, but that specific degrees of freedom can be selected to control the crack opening displacement. A more general solution that does not require a priori information on where the localization will take place, introduced by Gutiérrez (2004), is a constraint based on the global energy release rate in the framework of a geometrically linear continuum damage model, which was foundation for the class of dissipation based arclength models. This idea was later extended by Verhoosel et al. (2009) to account for geometrically linear plasticity and geometrically nonlinear damage. Van der Meer et al. (2010) extended the constraint equation to account also for the presence of thermal strains in the dissipation process. A common element among all mentioned arclength formulations is that they work with a fixed unit load vector and a predefined constraint equation. For off-axis loading at constant strain-rate on an RVE, such unit force vector and constraint can also be defined, depending on the mapping between local and global coordinates. In geometric nonlinear context which is relevant for shear loading of polymer composites, however, this mapping will change as a consequence of deformations.

In this study a strain-rate based arclength model is proposed. The constraint equation is constructed such that the deformation pattern of the RVE satisfies that the strain-rate in the global loading direction equals a prescribed value. To exactly capture the finite strains, the orientation of the RVE is updated, followed by a change in the unit force vector applied in the arclength method. Closed-form expressions for the unit force components are derived.

In the next section, the formulation for the strain-rate based arclength model is presented, first accounting for geometric nonlinear effects in a general nonlinear framework, and then reduced to a small strain version. After that, the Eindhoven Glassy Polymer (EGP) constitutive law that is used for the bulk (matrix) part of the composite material is introduced. Then a transversely isotropic material model is presented to simulate the response of the reinforcement - in this study carbon fibers. Subsequently the model is validated through examples on the rate-dependent isotropic material (EGP) and the transversely isotropic material. Eventually the off-axis response of a fiber reinforced composite material with thermoplastic matrix is simulated to demonstrate the envisioned use case of the proposed model.

2. Formulation

2.1. Problem statement

A composite material with unidirectional reinforcement is subjected to a constant strain-rate $\dot{\epsilon}_{yy}$ at uniaxial stress conditions, Fig. 1(left). The uniaxial loading will make the material undergo the deformation shown in Fig. 1(middle). Finite strains are allowed to take place, meaning that the local coordinate frame aligned with the fibers changes orientation from the initial angle θ_0 to a new angle θ_1. Given the angle θ_1, transformation of the stress state from global to local frame of reference results in the Cauchy stress components shown in Fig. 1(right). We aim to simulate this experiment with an RVE that is a 3D slice with random fiber distribution and periodic boundary conditions (Van der Meer, 2016), picked from the composite lamina, where one axis of the RVE is aligned with the reinforcement direction, Fig. 2. The implementation of periodic boundary conditions is explained in the appendix. Unlike a 2D RVE in the plane perpendicular to the fibers, the 3D slice enables representation of the stress state that is encountered in the off-axis loading of composites.

The kinematic relations between microscopic displacements and homogenized strain are calculated numerically, following displacements of the master nodes of the RVE. Displacement components of the master nodes not indicated in Fig. 2 are set to zero. Master node 0 is fixed to prevent rigid-body translations. It should be noted that we are not applying a macroscopic strain tensor on the RVE to define Dirichlet boundary conditions, in which case rigid-body rotations would be a priori prevented. Contrary to this, we are imposing forces on the RVE as part of the arclength methodology. Hence, it is necessary to fix three more degrees of freedom to prevent rigid-body rotations. Fixing master node 1 in $\boldsymbol{e}_2$ and $\boldsymbol{e}_3$ directions ensures that the fibers remain oriented in $\boldsymbol{e}_1$ direction. The vector $\boldsymbol{e}_2$ remains perpendicular to $\boldsymbol{e}_1$ and therefore does not necessarily stay parallel to the line between master nodes 0 and 2.

The formulation of the model is derived such that the deformation pattern and stress state of the RVE in the local frame of reference are equivalent to the global state of deformation and stress in the lamina, see Fig. 1. With the proposed model it is possible to analyze UD composite systems on the microlevel, accounting for different orientations of the reinforcement and a predefined strain-rate, while using the same initial geometry of the RVE. The derived model is valid for both tension and compression. Furthermore, the framework is independent of the material model applied to represent nonlinear processes in the composite constituents. Beside capturing the rate-dependent (visco-plastic) effects in the material, it is also possible to include damage mechanisms in the RVE model. For example, a cohesive surface methodology or a smeared crack model can be applied to represent degradation in the material. However, not all failure mechanisms may be represented by the thin slice RVE. The case of fiber kinking or fiber pull-out would require a longer piece of material to capture longitudinal variations in the fiber deformation and, therefore, cannot be simulated with the proposed model.

In the following, the general nonlinear framework of the model is introduced. Afterwards, the small strain version of the model that is simpler to implement is presented. In the numerical examples, the loss in accuracy when using the small strain version will be assessed.

2.2. Arclength control method

The discrete equilibrium equation of the RVE, in the absence of cracks and body forces, can be written in Voigt notation as follows:

$$\int_{\Omega} \mathbf{B}^{\mathrm{T}}(\mathbf{a})\boldsymbol{\sigma}(\mathbf{a})d\Omega = \int_{\Gamma_t} \mathbf{N}^{\mathrm{T}}\mathbf{t}_{\mathrm{p}}d\Gamma \tag{1}$$

where $\mathbf{B}$ is the strain - nodal displacement matrix, $\boldsymbol{\sigma}$ is the Cauchy stress, $\mathbf{N}$ is the shape function matrix, $\mathbf{t}_{\mathrm{p}}$ is the prescribed external traction, and $\mathbf{a}$ is the vector of nodal displacements. The left hand side of this equation represents the internal nodal force vector $\mathbf{f}_{\mathrm{int}}$, whereas the right hand side stands for the external force vector $\mathbf{f}_{\mathrm{ext}}$, leading to:

$$\mathbf{f}_{\mathrm{int}}(\mathbf{a}) = \mathbf{f}_{\mathrm{ext}}(\mathbf{a}) \tag{2}$$

In the light of the arclength control method, $\mathbf{f}_{\mathrm{ext}}$ is written as the product of the load factor λ and the unit force vector $\hat{\mathbf{f}}$:

$$\mathbf{f}_{\mathrm{ext}}(\mathbf{a}) = \lambda\hat{\mathbf{f}}(\mathbf{a}) \tag{3}$$

In the present case, the vector $\hat{\mathbf{f}}$ depends on the deformation state and, therefore, is a function of the nodal displacements. With periodic boundary conditions implemented as linear constraints, the right hand side vector of Eq. (1) translates to a force vector with nonzero values on the entries associated with the master nodes as shown in Fig. 2.

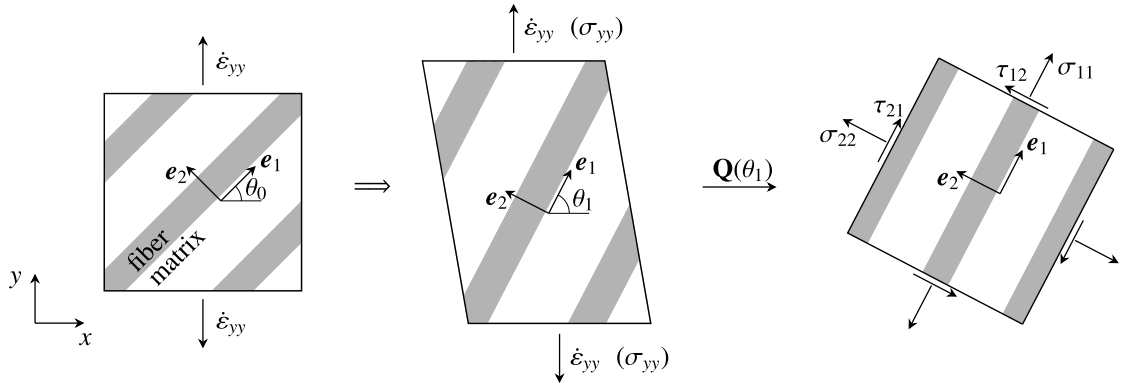

Fig. 1. Strain-rate imposed on unidirectional composite material (left); deformed material due to uniaxial loading (middle); Cauchy stresses in local coordinate system (right).

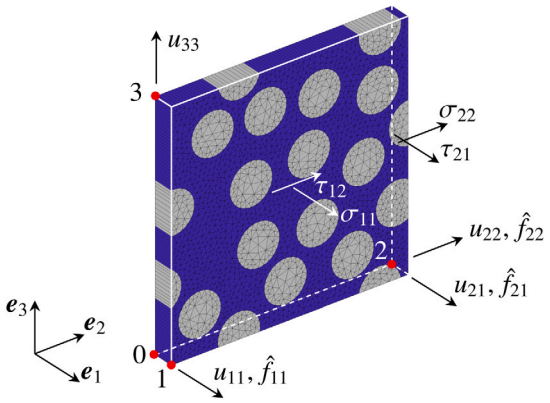

Fig. 2. RVE with active displacements u_{ij} and applied unit force components $\hat{f}_{ij}$ on master nodes 0, 1, 2, 3.

The system of Eqs. (2) consists of N equations and counts $N+1$ unknowns (N nodal displacements plus the load factor λ), rendering the system indeterminate. In order to solve this issue, a path following constraint equation is added, which in the general case has the form:

$$g(\mathbf{a}, \lambda, \tau) = 0 \tag{4}$$

where τ is an arclength parameter that defines the calculation step size. The combination of Eqs. (2)–(4) forms the augmented system of equations:

$$\begin{bmatrix} \mathbf{f}_{\text{int}} - \lambda \hat{\mathbf{f}} \\ g \end{bmatrix} = \begin{bmatrix} \mathbf{0} \\ 0 \end{bmatrix} \tag{5}$$

This is solved for the unknown nodal displacements and the load factor λ following the linearized Newton–Raphson procedure:

$$\begin{bmatrix} \mathbf{f}_{\text{int},j} + \frac{\partial \mathbf{f}_{\text{int}}}{\partial \mathbf{a}} d\mathbf{a}_{j+1} - \lambda_j \hat{\mathbf{f}} - d\lambda_{j+1} \hat{\mathbf{f}} \\ g_j + \left(\frac{\partial g}{\partial \mathbf{a}}\right)^{\mathrm{T}} d\mathbf{a}_{j+1} + \left(\frac{\partial g}{\partial \lambda}\right) d\lambda_{j+1} \end{bmatrix} = \begin{bmatrix} \mathbf{0} \\ 0 \end{bmatrix} \tag{6}$$

The solution at iteration $j+1$ is obtained by solving:

$$\begin{bmatrix} \mathbf{K} & -\hat{\mathbf{f}} \\ \mathbf{h}^{\mathrm{T}} & s \end{bmatrix} \begin{bmatrix} d\mathbf{a}_{j+1} \\ d\lambda_{j+1} \end{bmatrix} = \begin{bmatrix} \mathbf{0} \\ 0 \end{bmatrix} \tag{7}$$

where the tangent stiffness of the system $\mathbf{K}$, vector $\mathbf{h}$ and scalar s are defined as:

$$\mathbf{K} = \frac{\partial \mathbf{f}_{\text{int}}}{\partial \mathbf{a}}, \mathbf{h} = \frac{\partial g}{\partial \mathbf{a}}, s = \frac{\partial g}{\partial \lambda} \tag{8}$$

In this paper a two-stage solution procedure, first introduced by Ramm (1981) and Crisfield (1982), and later elaborated by De Borst et al. (2012), is used to update the unknown variables. At iteration $j+1$ the partial contributions to the nodal displacements are calculated as:

$$\begin{aligned} d\mathbf{a}^{\mathrm{I}}_{j+1} &= \mathbf{K}^{-1} \hat{\mathbf{f}} \\ d\mathbf{a}^{\mathrm{II}}_{j+1} &= \mathbf{K}^{-1} \mathbf{r}_j \end{aligned} \tag{9}$$

where $\mathbf{r}_j$ is the residual force vector at iteration j. Eq. (9) is followed by calculating an iterative increment to the load factor:

$$d\lambda_{j+1} = -\frac{g_j + \mathbf{h}^{\mathrm{T}} d\mathbf{a}^{\mathrm{II}}_{j+1}}{s + \mathbf{h}^{\mathrm{T}} d\mathbf{a}^{\mathrm{I}}_{j+1}} \tag{10}$$

to finally get the total iterative contribution to the nodal displacements:

$$d\mathbf{a}_{j+1} = d\lambda_{j+1} d\mathbf{a}^{\mathrm{I}}_{j+1} + d\mathbf{a}^{\mathrm{II}}_{j+1} \tag{11}$$

In Eq. (6) it is assumed that $\partial \hat{\mathbf{f}} / \partial \mathbf{a} = \mathbf{0}$, while in the present case the unit force vector does become a function of the deformation. In order to keep optimal convergence, while avoiding further complications in the formulation, the unit force vector $\hat{\mathbf{f}}$ is only updated at the beginning of the time step, i.e.:

$$\hat{\mathbf{f}}^n = \hat{\mathbf{f}}(\mathbf{a}^{n-1}) \tag{12}$$

2.3. Arclength constraint equation

The constraint equation of the model is derived from a relation between the RVE deformation gradient in the local coordinate system $\bar{\mathbf{F}}$ and the deformation gradient of the UD composite material in the global frame $\mathbf{F}$. To this end, the RVE with periodic boundary conditions, whose initial orientation with respect to the global x-axis defines the angle θ_0, is picked from the composite lamina, see Fig. 3(left) for top view and Fig. 2 for 3D view. Due to the applied loading, the initial RVE denoted by the shape "a" will deform into the shape "b" defined by the deformation gradient $\hat{\mathbf{F}}$ in the original local frame, Fig. 3(right). The deformation gradient $\hat{\mathbf{F}}$ describes the exact same deformation as the global deformation gradient $\mathbf{F}$. The two are related through a transformation operation as:

$$\hat{\mathbf{F}} = \mathbf{Q}_0 \mathbf{F} \mathbf{Q}_0^{\mathrm{T}} \tag{13}$$

where the transformation matrix $\mathbf{Q}_0$ reads:

$$\mathbf{Q}_0 = \begin{bmatrix} \cos(\theta_0) & \sin(\theta_0) & 0 \\ -\sin(\theta_0) & \cos(\theta_0) & 0 \\ 0 & 0 & 1 \end{bmatrix} \tag{14}$$

A simulation performed on the RVE should resemble this actual deformation state. In the actual state of shape "b" it can be observed that the vector $\boldsymbol{e}_1$ that is tied to the RVE edge 0–1 rotates with an angle ϕ. However, inside the RVE, this rotation is by definition of the boundary

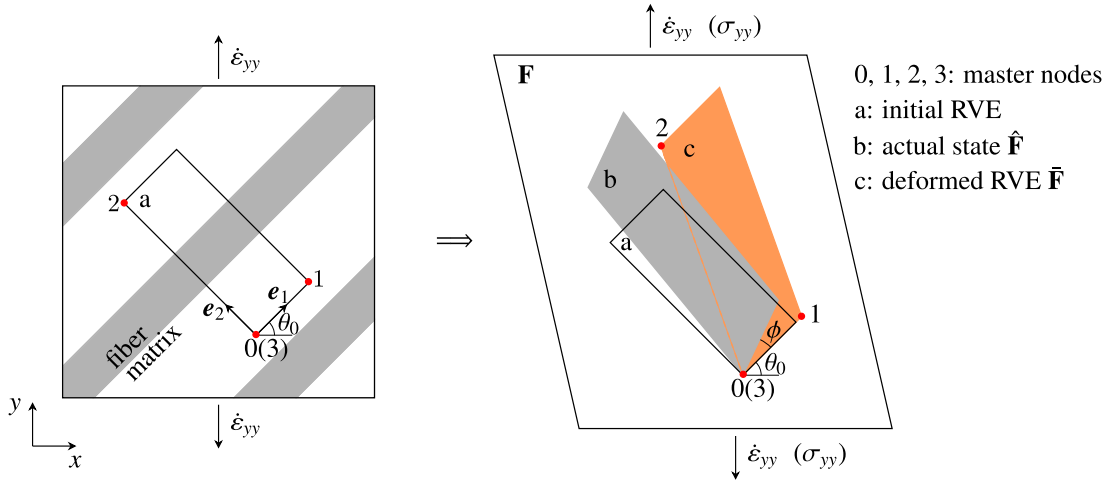

Fig. 3. RVE picked from composite lamina such that one side is parallel to the reinforcement (left); deformed RVE present in simulation and actual state it is in due to the applied loading (right).

conditions not described.[1] In order to relate the homogenized stresses in the RVE simulation to the stress in global frame, the magnitude of the rotation ϕ needs to be determined from the RVE simulation. This is achieved by considering that the RVE present in the simulation is in shape "c", with deformation gradient $\bar{\mathbf{F}}$, see Fig. 3(right). The deformation gradient $\bar{\mathbf{F}}$ is then related to the actual state $\hat{\mathbf{F}}$ by a rigid rotation:

$$\hat{\mathbf{F}} = \mathbf{R}(\phi)\bar{\mathbf{F}} \tag{15}$$

where the rotation tensor $\mathbf{R}$ has the following form:

$$\mathbf{R} = \begin{bmatrix} \cos(\phi) & -\sin(\phi) & 0 \\ \sin(\phi) & \cos(\phi) & 0 \\ 0 & 0 & 1 \end{bmatrix} \tag{16}$$

With the imposed Dirichlet boundary conditions and active displacements shown in Fig. 2, the homogenized deformation gradient of the RVE is:

$$\bar{\mathbf{F}} = \begin{bmatrix} \bar{F}_{11} & \bar{F}_{12} & 0 \\ 0 & \bar{F}_{22} & 0 \\ 0 & 0 & \bar{F}_{33} \end{bmatrix} = \begin{bmatrix} 1 + \frac{u_{11}}{l_1^0} & \frac{u_{21}}{l_2^0} & 0 \\ 0 & 1 + \frac{u_{22}}{l_2^0} & 0 \\ 0 & 0 & 1 + \frac{u_{33}}{l_3^0} \end{bmatrix} \tag{17}$$

such that u_{ij} is the displacement on master node i in direction j, whereas l_i^0 is the initial length of the RVE in direction i.

Combining Eqs. (15) and (13) it is possible to relate $\mathbf{F}$ to $\bar{\mathbf{F}}$ as:

$$\mathbf{F} = \mathbf{Q}_0^{\mathrm{T}}\mathbf{R}\bar{\mathbf{F}}\mathbf{Q}_0 \tag{18}$$

Taking the fact that $\mathbf{Q}_0^{\mathrm{T}}\mathbf{R} = \mathbf{Q}_1^{\mathrm{T}}$, Eq. (18) can be rewritten as:

$$\mathbf{F} = \mathbf{Q}_1^{\mathrm{T}}\bar{\mathbf{F}}\mathbf{Q}_0 \tag{19}$$

Here, the transformation matrix $\mathbf{Q}_1$ depends on the angle $\theta_1 = \theta_0 + \phi$, see Fig. 3(right):

$$\mathbf{Q}_1 = \begin{bmatrix} \cos(\theta_1) & \sin(\theta_1) & 0 \\ -\sin(\theta_1) & \cos(\theta_1) & 0 \\ 0 & 0 & 1 \end{bmatrix} \tag{20}$$

The angle ϕ marks the change in orientation of the RVE with respect to the global frame of reference from the angle θ_0 to the angle θ_1. This change in the orientation stems from the finite deformation that the RVE undergoes, and is present also for an isotropic material: if we consider from the tensile specimen a slice of material initially aligned with an angle θ_0 unequal to 0° or 90°, the orientation of this slice will change as the material deforms, see Fig. 4. The shear deformation of an orthotropic material under uniaxial loading further contributes to this reorientation. In order to compute ϕ from $\bar{\mathbf{F}}$ we make use of the knowledge on the deformation gradient $\mathbf{F}$, which has $F_{yx} = 0$. We assume that the experimental boundary conditions are such that rotation of the specimen edges on which the stress is applied is prevented, while relative transverse translation of these edges is free. The specimen then deforms into the shape of the outermost parallelogram shown in Fig. 3. With loading in y-direction, this implies that the gradient of u_y in x-direction is equal to zero, while the gradient of u_x in y-direction can take a nonzero value. Therefore, $F_{yx} = 0$ and $\mathbf{F}$ has the following form:

$$\mathbf{F} = \begin{bmatrix} F_{xx} & F_{xy} & 0 \\ 0 & F_{yy} & 0 \\ 0 & 0 & F_{zz} \end{bmatrix} \tag{21}$$

An expression for the angle ϕ is determined by equating the F_{yx} component of the global deformation gradient $\mathbf{F}$ from Eq. (18) to zero.

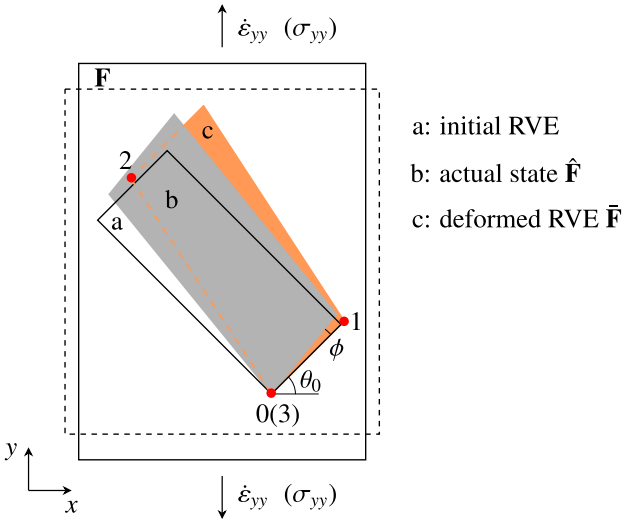

Fig. 4. Deformed RVE present in simulation and actual state it is in due to the applied loading on isotropic material.

[1] An assumption that the master node 2 does not move in the local direction 1, while the node 1 moves in the direction 2, would result in different expressions for the RVE kinematics, but the overall simulation results would be the same if a derivation similar to the one outlined here is followed.

This condition leads to the following expression for ϕ:

$$\phi = \arctan\left(\frac{-\bar{F}_{11}c_0s_0 + \bar{F}_{12}s_0^2 + \bar{F}_{22}c_0s_0}{\bar{F}_{11}c_0^2 - \bar{F}_{12}c_0s_0 + \bar{F}_{22}s_0^2}\right) \tag{22}$$

where s_0 and c_0 denote $\sin(\theta_0)$ and $\cos(\theta_0)$.

In order to derive the strain-rate based constraint equation, the F_{yy} component of the lamina deformation gradient $\mathbf{F}$ is picked from Eq. (19), and equated to the corresponding value imposed from the input:

$$g = 0: \quad \underbrace{\bar{F}_{11}s_0s_1 + \bar{F}_{22}c_0c_1 + \bar{F}_{12}c_0s_1}_{F_{yy}\text{ calculated from RVE}} - \underbrace{\exp(\varepsilon_{yy}^{n-1} + \dot{\varepsilon}_{yy}\Delta t)}_{F_{yy}\text{ imposed from input}} = 0 \tag{23}$$

where s_1 and c_1 stand for $\sin(\theta_1)$ and $\cos(\theta_1)$, ε_{yy}^{n-1} is the total strain in the loading direction from last converged time step, $\dot{\varepsilon}_{yy}$ is the strain-rate imposed in the analysis, and Δt is the time increment. The F_{yy} term imposed from the input derives from the true-strain definition in the loading direction:

$$\varepsilon_{yy} = \ln\left(\frac{l_y^0 + u_{yy}}{l_y^0}\right) = \ln(F_{yy}) \tag{24}$$

in which l_y^0 is the initial length of the lamina in the loading direction, and u_{yy} is the displacement in the same direction. The true strain in the loading direction at the current time step is numerically represented as:

$$\varepsilon_{yy}^{n} = \varepsilon_{yy}^{n-1} + \dot{\varepsilon}_{yy}\Delta t \tag{25}$$

which after substitution in Eq. (24) yields:

$$F_{yy}^{n} = \exp(\varepsilon_{yy}^{n-1} + \dot{\varepsilon}_{yy}\Delta t) \tag{26}$$

The term $\dot{\varepsilon}_{yy}\Delta t$ plays the role of the arclength parameter in Eq. (4) and ensures that the deformation pattern of the RVE corresponds to the global strain-rate imposed in the analysis.

By replacing the $\bar{F}_{ij}$ components in Eq. (23) with corresponding expressions from Eq. (17), the constraint equation $g = 0$ is expressed in terms of nodal displacements:

$$\left(1 + \frac{u_{11}}{l_1^0}\right)s_0s_1 + \left(1 + \frac{u_{22}}{l_2^0}\right)c_0c_1 + \frac{u_{21}}{l_2^0}c_0s_1 - \exp(\varepsilon_{yy}^{n-1} + \dot{\varepsilon}_{yy}\Delta t) = 0 \tag{27}$$

It is obvious that the equation does not depend on the load factor λ. Therefore:

$$s = \frac{\partial g}{\partial \lambda} = 0 \tag{28}$$

An assumption is introduced that the angle ϕ is calculated given the deformation state from last converged time step. With this, it is true within each time step that:

$$\frac{\partial \cos(\theta_1)}{\partial \mathbf{a}} = \frac{\partial \sin(\theta_1)}{\partial \mathbf{a}} = \mathbf{0} \tag{29}$$

This simplifies the linearization of the constraint equation with respect to the displacements of the master nodes, such that:

$$\mathbf{h}^{\mathrm{T}} = \left(\frac{\partial g}{\partial \mathbf{a}}\right)^{\mathrm{T}} = \underbrace{\begin{bmatrix}0 & 0\end{bmatrix}}_{\text{node 0}} \underbrace{\begin{bmatrix}s_0s_1/l_1^0 & 0\end{bmatrix}}_{\text{node 1}} \underbrace{\begin{bmatrix}c_0s_1/l_2^0 & c_0c_1/l_2^0\end{bmatrix}}_{\text{node 2}} \underbrace{\begin{bmatrix}0 & 0\end{bmatrix}}_{\text{node 3}} \tag{30}$$

2.4. Unit force vector

Another essential ingredient of every arclength control method is the unit force vector $\hat{\mathbf{f}}$. It is applied at nodes where the external force level needs to be controlled. In the context of a uniaxial test, $\hat{\mathbf{f}}$ should correspond to unit applied stress. Since the model aims at capturing finite strains in the material, the relative magnitude of the forces defined on the master nodes and the homogenized applied stress cannot be set on the initial configuration of the RVE, in the sense of small strain theory. The geometrically nonlinear effect on the unit force vector is twofold. Firstly, the change in the initial geometry of the RVE from the shape "a" to the shape "c", see Fig. 3, asks for an update in $\hat{\mathbf{f}}$. Secondly, the actual change in orientation of the RVE for the angle ϕ introduces another geometric effect to the unit force vector. With this in mind it becomes apparent that $\hat{\mathbf{f}}$ depends on the deformation state of the RVE, and is a function of the nodal displacements.

The unit force vector is applied on the RVE such that the corresponding stress state is equivalent to the global stress state of the material, see Fig. 1. The components of this vector are derived considering the formula for internal nodal forces (Belytschko et al., 2014), for a single hexahedral finite element with the size and orientation of the initial RVE domain in the local coordinate system:

$$\bar{\mathbf{f}}_{\text{int}} = \int_{\Omega_0} \bar{\mathbf{B}}_0^{\mathrm{T}}\bar{\mathbf{F}}^{-1}\bar{\boldsymbol{\sigma}}\bar{J}\,d\Omega_0 \tag{31}$$

where $\bar{\mathbf{B}}_0$ is the strain - nodal displacement matrix defined for trilinear shape functions defined over the whole RVE domain, while $\bar{J}$ is the determinant of the RVE deformation gradient $\bar{\mathbf{F}}$.[2] The Cauchy stress tensor $\bar{\boldsymbol{\sigma}}$ comes from the transformation of the global stress state to the local frame, see Fig. 1:

$$\bar{\boldsymbol{\sigma}} = \mathbf{Q}_1\boldsymbol{\sigma}\mathbf{Q}_1^{\mathrm{T}} = \sigma_{yy}\begin{bmatrix}s_1^2 & c_1s_1 & 0\\ c_1s_1 & c_1^2 & 0\\ 0 & 0 & 0\end{bmatrix} = \begin{bmatrix}\sigma_{11} & \tau_{12} & 0\\ \tau_{21} & \sigma_{22} & 0\\ 0 & 0 & 0\end{bmatrix} \tag{32}$$

For the problem at hand, the load factor λ is identical to the magnitude of the stress component in the global loading direction:

$$\lambda \equiv \sigma_{yy} \tag{33}$$

The stress state of Eq. (32) and the imposed Dirichlet boundary conditions imply that three components of the unit force vector acting on the RVE are nonzero, see Fig. 2. Expressions for these components follow from evaluating Eq. (31):

$$\begin{aligned}\hat{f}_{11} &= A_1^0\bar{J}\left(\frac{s_1^2}{\bar{F}_{11}} - c_1s_1\frac{\bar{F}_{12}}{\bar{F}_{11}\bar{F}_{22}}\right)\\ \hat{f}_{21} &= A_2^0\bar{J}\frac{c_1s_1}{\bar{F}_{22}}\\ \hat{f}_{22} &= A_2^0\bar{J}\frac{c_1^2}{\bar{F}_{22}}\end{aligned} \tag{34}$$

Here $\hat{f}_{ij}$ is the unit force component on master node i in direction j, whereas A_i^0 represents an initial surface (side of the RVE) on which a corresponding stress component is acting. From Eq. (34) it is clear that $\hat{\mathbf{f}}$ depends on the deformation state of the RVE through its deformation gradient components, but also on a proper transformation that relies on the change in the RVE orientation through the angle ϕ, as needed for c_1 and s_1.

2.5. Implementation

Time discretization in Eq. (27) is exact and so far all equations are derived in the current configuration. The angles ϕ and hence θ_1 are a function of the current displacements. For a fully implicit formulation, ϕ would need to be updated every iteration, rendering the linearization of Eq. (6) inexact. To keep optimal convergence without the need to extend the arclength solution algorithm with additional linearization terms, the angle ϕ is only updated between time steps and in every time step the c_1, s_1 and $\bar{\mathbf{F}}$ in Eqs. (23) and (34) are based on the converged deformation from the previous time step.

The algorithmic details of the model, adjusted for the present case from De Borst et al. (2012), are summarized in Table 1. It is important

[2] The relevant quantities here are written in tensor notation, making $\bar{\mathbf{f}}_{\text{int}}$ matrix of the size Nnodes × 3, such that each row represents three components of the force vector at one node.

Table 1
Algorithm of the strain-rate based arclength model for time step n.

(1) set step size Δt; set $j = 0$, $\Delta \mathbf{a}_0 = 0$
(2) given $\bar{\mathbf{F}}^{n-1}$, compute ϕ from Eq. (22); set $\theta_1 = \theta_0 + \phi$
(3) update the unit force vector $\hat{\mathbf{f}}$, Eq. (34)
(4) compute the tangent stiffness matrix of the system $\mathbf{K}_j$
(5) set prescribed displacements
(6) compute $d\mathbf{a}^{\mathrm{I}}_{j+1}$ and $d\mathbf{a}^{\mathrm{II}}_{j+1}$, Eq. (9)
(7) compute $d\lambda_{j+1}$, Eq. (10)
(8) compute $\Delta \mathbf{a}_{j+1} = \Delta \mathbf{a}_j + d\lambda_{j+1} d\mathbf{a}^{\mathrm{I}}_{j+1} + d\mathbf{a}^{\mathrm{II}}_{j+1}$
(9) given $\Delta \mathbf{a}_{j+1}$, compute $\Delta \bar{\mathbf{F}}_{i,j+1}$ for every integration point
(10) compute deformation gradient $\bar{\mathbf{F}}_{i,j+1} = \Delta \bar{\mathbf{F}}_{i,j+1} \cdot \bar{\mathbf{F}}_i^{n-1}$ for every integration point
(11) given $\bar{\mathbf{F}}_{i,j+1}$, compute $\boldsymbol{\sigma}_{i,j+1}$ for every integration point
(12) compute the internal force vector $\mathbf{f}_{\mathrm{int},j+1}$
(13) check convergence Eq. (5); if converged go to the next time step, otherwise go to 4

to note that in these steps $\bar{\mathbf{F}}_i$ represents the deformation gradient at integration point i of the RVE, and is not to be confused with the deformation gradient $\mathbf{F}$ of the lamina as a whole, and the homogenized deformation gradient $\bar{\mathbf{F}}$ of the RVE as a whole.

2.6. Small strain version

The elaborated formulation does not impose any restriction on the kinematics relations and is considered as the general nonlinear framework. However, in many applications of practical interest structural components made of composites remain in the small strain regime, even in a failure event. Therefore it is relevant to show equations applicable in the range of small deformations which allow for a more straightforward implementation.

A first simplification comes from the fact that the angle ϕ remains close to zero in the case of a small strain deformation process. Correspondingly, the constraint Eq. (27) reduces to a new form:

$$\left(1 + \frac{u_{11}}{l_1^0}\right) s_0^2 + \left(1 + \frac{u_{22}}{l_2^0}\right) c_0^2 + \frac{u_{21}}{l_2^0} c_0 s_0 - \exp(\epsilon_{yy}^{n-1} + \dot{\epsilon}_{yy} \Delta t) = 0 \tag{35}$$

in which the transformation completely depends on the initial angle θ_0, see Fig. 3, through $\sin(\theta_0)$ and $\cos(\theta_0)$ terms.

Another simplification concerns the unit force vector, which in the event of small deformations will be the same in every time step:

$$\begin{aligned} \hat{f}_{11} &= A_1^0 s_0^2 \\ \hat{f}_{21} &= A_2^0 c_0 s_0 \\ \hat{f}_{22} &= A_2^0 c_0^2 \end{aligned} \tag{36}$$

Compared to Eq. (34) the terms in Eq. (36) do not depend on the components of the RVE deformation gradient $\bar{\mathbf{F}}$, which means that the right hand side of Eq. (1) is calculated on the initial configuration, in the small strain sense. Furthermore, the transformation is conducted with the constant angle θ_0.

These two simplifications mean that geometric nonlinear effects are neglected in the constraint equation and the unit force vector, and throughout the simulation the RVE is taken to be in the shape "a", see Fig. 3.

3. The Eindhoven glassy polymer constitutive model

In this section, the governing equations of the Eindhoven Glassy Polymer (EGP) model that is used to describe the matrix behavior in the composite material are summarized. The EGP model will also be used in a standalone manner in a single element test, to test the performance of the arclength model.

The EGP is an isotropic, elasto-viscoplastic, 3D constitutive law. It is based on the Eyring flow theory (Eyring, 1936), in the sense that an Eyring-based viscosity exponentially reduces with applied stress, also reducing the material relaxation time. Consequently, the plastic flow at yield is regarded as a stress-induced melting, and there is no need for an explicit yield surface.

Description of the formulation starts from the deformation gradient of a material point. Let that material point be integration point i whose deformation gradient is denoted with $\mathbf{F}_i$.[3] It is decomposed in the elastic and the plastic part (Senden et al., 2012):

$$\mathbf{F}_i = \mathbf{F}_{i\mathrm{e}} \cdot \mathbf{F}_{i\mathrm{p}} \tag{37}$$

The plastic deformation preserves volume, so that the volumetric change is purely elastic:

$$J_i = \det(\mathbf{F}_i) = \det(\mathbf{F}_{i\mathrm{e}}) \tag{38}$$

An additive decomposition of the Cauchy stress is assumed:

$$\boldsymbol{\sigma} = \boldsymbol{\sigma}_{\mathrm{h}} + \boldsymbol{\sigma}_{\mathrm{r}} + \boldsymbol{\sigma}_{\mathrm{s}} \tag{39}$$

where $\boldsymbol{\sigma}_{\mathrm{h}}$ is the hydrostatic component, $\boldsymbol{\sigma}_{\mathrm{r}}$ is the hardening stress, and $\boldsymbol{\sigma}_{\mathrm{s}}$ is the driving stress contribution. The hydrostatic stress depends on the bulk modulus κ and the change in volume J_i:

$$\boldsymbol{\sigma}_{\mathrm{h}} = \kappa(J_i - 1)\mathbf{I} \tag{40}$$

where $\mathbf{I}$ is the unit tensor. The hardening stress, explained as a rubber elastic response due to orienting of the entangled network, emerges as:

$$\boldsymbol{\sigma}_{\mathrm{r}} = G_{\mathrm{r}} \tilde{\mathbf{B}}^{\mathrm{d}} \tag{41}$$

in which G_{r} is the strain hardening modulus, and $\tilde{\mathbf{B}}^{\mathrm{d}}$ is the deviatoric part of the isochoric left Cauchy–Green deformation tensor:

$$\tilde{\mathbf{B}}^{\mathrm{d}} = \left(\tilde{\mathbf{F}}_i \cdot \tilde{\mathbf{F}}_i^{\mathrm{T}}\right)^{\mathrm{d}} = J_i^{-2/3} \left(\mathbf{F}_i \cdot \mathbf{F}_i^{\mathrm{T}}\right)^{\mathrm{d}} \tag{42}$$

The driving stress in the EGP model, ascribed to intermolecular interactions of the polymer, may also account for thermorheologically complex behavior (Klompen and Govaert, 1999). The deformation kinetics are then governed by multiple molecular processes, here denoted for two different ones as α and β:

$$\boldsymbol{\sigma}_{\mathrm{s}} = \boldsymbol{\sigma}_{\alpha} + \boldsymbol{\sigma}_{\beta} \tag{43}$$

In addition to this, every relaxation process may be represented by a spectrum of viscosities (or relaxation times) and corresponding shear moduli (Van Breemen et al., 2011). Mechanically this is achieved by a number of Maxwell elements connected in parallel:

$$\begin{aligned} \boldsymbol{\sigma}_{\mathrm{s}} &= \sum_{k=1}^{n} \boldsymbol{\sigma}_{\alpha,k} + \sum_{l=1}^{m} \boldsymbol{\sigma}_{\beta,l} \\ &= \sum_{k=1}^{n} G_{\alpha,k} \tilde{\mathbf{B}}^{\mathrm{d}}_{\mathrm{e}\alpha,k} + \sum_{l=1}^{m} G_{\beta,l} \tilde{\mathbf{B}}^{\mathrm{d}}_{\mathrm{e}\beta,l} \end{aligned} \tag{44}$$

In this equation, $G_{x,j}$ stands for the shear modulus of Maxwell element j belonging to process x, where x is either α or β. $\tilde{\mathbf{B}}^{\mathrm{d}}_{\mathrm{ex},j}$ is the elastic part of the isochoric, deviatoric left Cauchy–Green deformation tensor, that describes the deformation process in the spring of jth Maxwell element of the relaxation process x. Because of the time- and history-dependence of a polymer material, the elastic deformation measure is calculated by integrating the evolution equation of $\tilde{\mathbf{B}}_{\mathrm{ex},j}$:

$$\dot{\tilde{\mathbf{B}}}_{\mathrm{ex},j} = \left(\tilde{\mathbf{L}} - \mathbf{D}_{\mathrm{px},j}\right) \cdot \tilde{\mathbf{B}}_{\mathrm{ex},j} + \tilde{\mathbf{B}}_{\mathrm{ex},j} \cdot \left(\tilde{\mathbf{L}}^{\mathrm{T}} - \mathbf{D}_{\mathrm{px},j}\right) \tag{45}$$

where $\tilde{\mathbf{L}}$ is the isochoric velocity gradient. To solve the evolution equation for $\tilde{\mathbf{B}}_{\mathrm{ex},j}$, a constitutive relation is introduced for the plastic part of the rate of deformation tensor:

$$\mathbf{D}_{\mathrm{px},j} = \frac{\boldsymbol{\sigma}_{x,j}}{2\eta_{x,j}(\bar{\tau}_x, p, S_x)} \tag{46}$$

[3] $\mathbf{F}_i$ is the same as $\bar{\mathbf{F}}_i$ in Table 1, but for the sake of simplified notation the bar sign is omitted in this and the subsequent section.

Table 2
Material parameters of the EGP model.

κ [MPa]	G_r [MPa]	$\tau_{0\alpha}$ [MPa]	μ_α	$S_{a\alpha}$	$r_{0\alpha}$	$r_{1\alpha}$	$r_{2\alpha}$
5475	14.2	1.386	0.08	3	0.95	1	−5

$\mathbf{D}_{\mathrm{p}x,j}$ is given in the form of a non-Newtonian flow rule, such that the viscosity is a function of the equivalent stress, which is an Eyring-based feature. Additionally the viscosity depends on two other parameters, the hydrostatic pressure $p = -\mathrm{tr}(\boldsymbol{\sigma})/3$, and the thermodynamic state parameter S_x[4]:

$$\eta_{x,j} = \eta_{0x,j} \frac{\bar{\tau}_x/\tau_{0x}}{\sinh(\bar{\tau}_x/\tau_{0x})} \exp\left(\frac{\mu_x p}{\tau_{0x}}\right) \exp(S_x) \tag{47}$$

Here, $\eta_{x,j}$ is the viscosity in the dashpot of Maxwell element j as part of relaxation process x, $\eta_{0x,j}$ is the corresponding initial viscosity, τ_{0x} is the characteristic shear stress, while μ_x represents the pressure-dependency parameter. The equivalent stress is computed according to:

$$\bar{\tau}_x = \sqrt{\frac{1}{2}\boldsymbol{\sigma}_x : \boldsymbol{\sigma}_x} \tag{48}$$

The state parameter S_x takes into account the thermodynamical history of the polymer. In the EGP model, it is a product of two competing mechanisms: the aging parameter S_{ax}, and the softening function $R_{\gamma x}(\bar{\gamma}_\mathrm{p})$.

$$S_x(\bar{\gamma}_\mathrm{p}) = S_{ax} R_{\gamma x}(\bar{\gamma}_\mathrm{p}) \tag{49}$$

where $\bar{\gamma}_\mathrm{p}$ is the equivalent plastic strain. The state parameter initially has the value S_{ax} which causes an increase in the yield stress due to aging effects. On the other side, the softening function tends to reverse this process and bring it to mechanically rejuvenated reference state. $R_{\gamma x}(\bar{\gamma}_\mathrm{p})$ varies from 1 at the onset of yielding, to 0 at fully rejuvenated state. This implies that, in the same range, the state parameter S_x varies from S_{ax} to 0. The softening function, included in the EGP model by Klompen et al. (2005), is represented as a modified Carreau–Yasuda function:

$$R_{\gamma x}(\bar{\gamma}_\mathrm{p}) = \left\{ \frac{1 + [r_{0x}\exp(\bar{\gamma}_\mathrm{p})]^{r_{1x}}}{1 + r_{0x}^{r_{1x}}} \right\}^{\frac{r_{2x}-1}{r_{1x}}} \tag{50}$$

Fitting parameters r_{0x}, r_{1x}, r_{2x} are usually taken the same for both relaxation processes. The equivalent plastic strain is calculated by numerically integrating the rate of equivalent plastic strain:

$$\dot{\bar{\gamma}}_\mathrm{p} = \frac{\bar{\tau}_{\alpha,1}}{\eta_{\alpha,1}}, \quad \bar{\tau}_{\alpha,1} = \sqrt{\frac{1}{2}\boldsymbol{\sigma}_{\alpha,1} : \boldsymbol{\sigma}_{\alpha,1}} \tag{51}$$

It is assumed that accumulation of the equivalent plastic strain is driven by the evolution of the mode with the highest initial viscosity. Usually this is the viscosity of the first Maxwell element of the α process $\eta_{\alpha,1}$.

Input data for the EGP model as used in this paper are listed in Tables 2 and 3. The data correspond to polyether ether ketone (PEEK) material. Only the relaxation process α is considered.

4. Transversely isotropic constitutive model

In this study carbon fibers are considered as reinforcement, where the carbon fibers themselves have transversely isotropic elastic properties. The constitutive law selected to model the carbon fibers is the hyperelastic, transversely isotropic material model developed by Bonet and Burton (1998). The constitutive law derives from the strain energy density function, that is split in an isotropic and a transversely isotropic component:

$$\Psi(\mathbf{C}) = \Psi_{\mathrm{iso}}(\mathbf{C}) + \Psi_{\mathrm{tri}}(\mathbf{C}) \tag{52}$$

[4] There are versions of the EGP model where the viscosity depends on additional parameters, see e.g. Senden et al. (2012).

Table 3
Relaxation spectrum of the EGP model.

x, j	$G_{x,j}$ [MPa]	$\eta_{0x,j}$ [MPa·s]
$\alpha, 1$	721.05	$7.5900 \cdot 10^{21}$
$\alpha, 2$	275.88	$4.2510 \cdot 10^{20}$
$\alpha, 3$	31.77	$1.2852 \cdot 10^{19}$
$\alpha, 4$	60.19	$9.2160 \cdot 10^{18}$
$\alpha, 5$	49.95	$2.9562 \cdot 10^{18}$
$\alpha, 6$	43.47	$9.9600 \cdot 10^{17}$
$\alpha, 7$	31.35	$2.7600 \cdot 10^{17}$
$\alpha, 8$	29.26	$9.9360 \cdot 10^{16}$
$\alpha, 9$	34.90	$4.5990 \cdot 10^{16}$
$\alpha, 10$	57.89	$1.1358 \cdot 10^{16}$
$\alpha, 11$	53.30	$4.3782 \cdot 10^{14}$
$\alpha, 12$	41.80	$1.4370 \cdot 10^{13}$
$\alpha, 13$	39.08	$5.6358 \cdot 10^{11}$
$\alpha, 14$	3.20	$1.9254 \cdot 10^{10}$
$\alpha, 15$	36.58	$9.1980 \cdot 10^{8}$
$\alpha, 16$	2.36	$2.4804 \cdot 10^{7}$
β, –	–	–

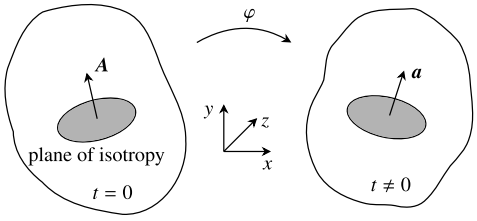

Fig. 5. Preferential stiffness direction $\boldsymbol{A}$ of the transversely isotropic material model maps to vector $\boldsymbol{a}$ upon deformation process.

The strain energy function refers to any material point in the initial configuration. Let a material point represent an integration point i whose deformation gradient is denoted with $\mathbf{F}_i$. With this, the right Cauchy–Green deformation tensor reads:

$$\mathbf{C} = \mathbf{F}_i^{\mathrm{T}}\mathbf{F}_i \tag{53}$$

The isotropic strain energy function used in this paper is a neo-Hookean potential of the form presented in, e.g., (Belytschko et al., 2014):

$$\Psi_{\mathrm{iso}} = \frac{\mu}{2}(I_1 - 3) - \mu\ln(J_i) + \frac{\lambda}{2}\left[\ln(J_i)\right]^2 \tag{54}$$

where I_1 is the trace of $\mathbf{C}$, J_i is the determinant of $\mathbf{F}_i$, λ and μ are material constants. The corresponding strain energy function in the reference paper (Bonet and Burton, 1998) assumes $(J_i - 1)^2$ instead of $[\ln(J_i)]^2$ in Eq. (54). The transversely isotropic potential is constructed as:

$$\Psi_{\mathrm{tri}} = \left[\alpha + \beta(I_1 - 3) + \gamma(I_4 - 1)\right](I_4 - 1) - \frac{1}{2}\alpha(I_5 - 1) \tag{55}$$

Here α, β and γ denote material constants, whereas the pseudo invariants I_4 and I_5 are defined as:

$$\begin{aligned} I_4 &= \boldsymbol{A} \cdot \mathbf{C}\boldsymbol{A} \\ I_5 &= \boldsymbol{A} \cdot \mathbf{C}^2\boldsymbol{A} \end{aligned} \tag{56}$$

so that the vector $\boldsymbol{A}$ signifies the preferential stiffness direction of the material in the initial configuration, Fig. 5. Upon deformation $\boldsymbol{A}$ maps to vector $\boldsymbol{a}$, the preferential stiffness direction in the current configuration:

$$\boldsymbol{a} = \mathbf{F}_i\boldsymbol{A} \tag{57}$$

Knowing the strain energy density function, the second Piola–Kirchhoff stress emerges as:

$$\mathbf{S} = 2\frac{\partial \Psi}{\partial \mathbf{C}} \tag{58}$$

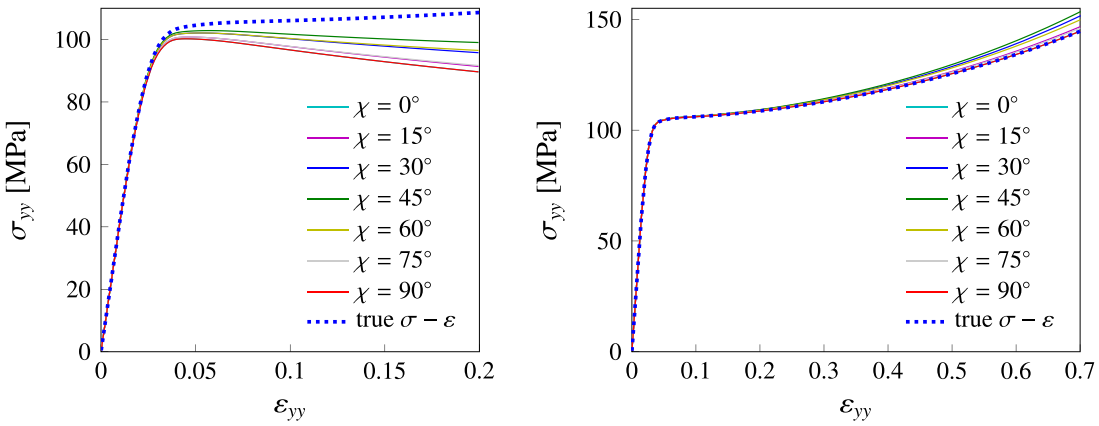

Fig. 6. The EGP response for $\dot{\varepsilon}_{yy} = 10^{-4}/\text{ s}$ with the small strain version (left); with the nonlinear version with $\phi = 0$ (right).

Table 4
Material parameters of the transversely isotropic constitutive law.

E_1 [GPa]	E_2 [GPa]	G_{12} [GPa]	ν_{12}	ν_{23}
125	15	45	0.05	0.3

This stress measure can be pushed forward to obtain expressions for the Cauchy stress contributions:

$$\boldsymbol{\sigma}_{\text{iso}} = \frac{\mu}{J_i}(\mathbf{B} - \mathbf{I}) + \frac{\lambda}{J_i}\ln(J_i)\mathbf{I} \tag{59}$$

and:

$$\boldsymbol{\sigma}_{\text{tri}} = J_i^{-1}\{2\beta(I_4-1)\mathbf{B}+2[\alpha+\beta(I_1-3)+2\gamma(I_4-1)]\boldsymbol{a}\otimes\boldsymbol{a}-\alpha(\mathbf{B}\boldsymbol{a}\otimes\boldsymbol{a}+\boldsymbol{a}\otimes\mathbf{B}\boldsymbol{a})\} \tag{60}$$

with the pseudo invariant $I_4 = \boldsymbol{a}\cdot\boldsymbol{a}$. In Eqs. (59) and (60) $\mathbf{B}$ represents the left Cauchy–Green deformation tensor.

The constants in the expressions for the strain energy potentials and stress tensors in this paper are slightly modified from this in the reference paper (Bonet and Burton, 1998). Here it is assumed that the Poisson ratio in the plane of isotropy, marked by ν_{23}, is different from the Poisson ratio, ν_{12}, for the planes orthogonal to the isotropic plane. This assumption leads to the following expressions for the constants:

$$\begin{aligned}
n &= \frac{E_1}{E_2}\\
m &= 1 - \nu_{23} - 2n\nu_{12}^2\\
\lambda &= \frac{E_2(\nu_{23} + n\nu_{12}^2)}{m(1+\nu_{23})}\\
\mu &= \frac{E_2}{2(1+\nu_{23})}\\
\alpha &= \mu - G_{12}\\
\beta &= \frac{E_2(\nu_{12} + \nu_{23}\nu_{12} - \nu_{23} - n\nu_{12}^2)}{4m(1+\nu_{23})}\\
\gamma &= \frac{E_1(1-\nu_{23})}{8m} - \frac{\lambda+2\mu}{8} + \frac{\alpha}{2} - \beta
\end{aligned} \tag{61}$$

where E_1 is the Young's modulus in preferential stiffness direction, E_2 and ν_{23} define behavior of the material in the plane of isotropy, while the shear stiffness G_{12} and Poisson's ratio ν_{12} define the behavior in planes perpendicular to that. In the case of $\nu_{12} = \nu_{23}$ the expressions in Eq. (61) reduce to those in Bonet and Burton (1998). The material parameters utilized in this study are listed in Table 4.

5. Examples

The strain-rate based arclength model has been tested on several examples, in order to prove the validity of the formulation. The aim is to check whether the model properly accounts for different orientation of the load relative to the orientation of the reinforcement, i.e., different off-axis angles, captures finite strains exactly, and reproduces the rate-dependency of the material. Where appropriate, the distinction is made between results obtained by applying the small strain version of the model and the general nonlinear framework. In the following, the angle χ denotes an initial off-axis angle between load direction and fiber direction, which from Fig. 3 reads as:

$$\chi = 90° - \theta_0 \tag{62}$$

The stress–strain curves show the corresponding values in the global loading direction, see Fig. 1. Those related to the arclength model have been generated making use of the fact that σ_{yy} is equal to the load factor λ of the arclength model, while for every time step ε_{yy} is updated with Eq. (25).

The first example is a homogeneous RVE with an isotropic constitutive law, see Fig. 4. For the isotropic material model, no matter what is the considered off-axis angle, the stress–strain response must be the same. The RVE with the EGP material model is subjected to constant strain-rate $\dot{\varepsilon}_{yy} = 10^{-4}/\text{ s}$, and several different off-axis angles are considered, covering the range from 0° to 90°. With the computational efficiency in mind, the analysis has been done on a single hexahedral finite element. Still, in the homogeneous RVE, one can expect to find the same results, for any number of finite elements in the mesh. Fig. 6(left) shows results in case the small strain version of the arclength model with Eqs. (35) and (36) is used. Here the unit force vector is not updated for the previous deformation in the RVE and also there is no change in the orientation of the RVE for the angle

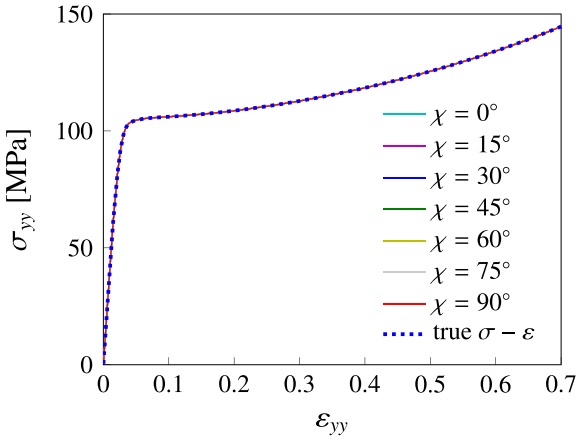

Fig. 7. The EGP response for $\dot{\varepsilon}_{yy} = 10^{-4}/\text{ s}$ with the general nonlinear framework.

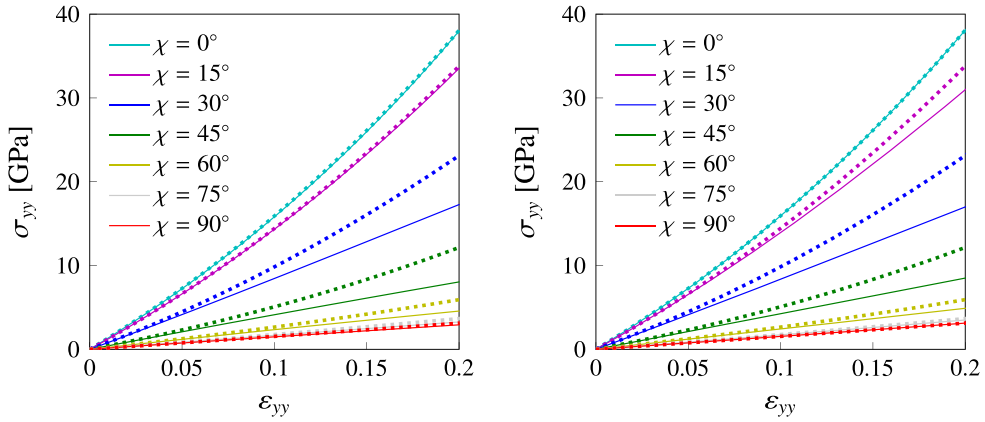

Fig. 8. Response of the transversely isotropic material for $\dot{\varepsilon}_{yy} = 10^{-4}/\,\mathrm{s}$ with the small strain version (left); with the nonlinear version with $\phi = 0$ (right); solid lines - the arclength model, dotted lines - reference.

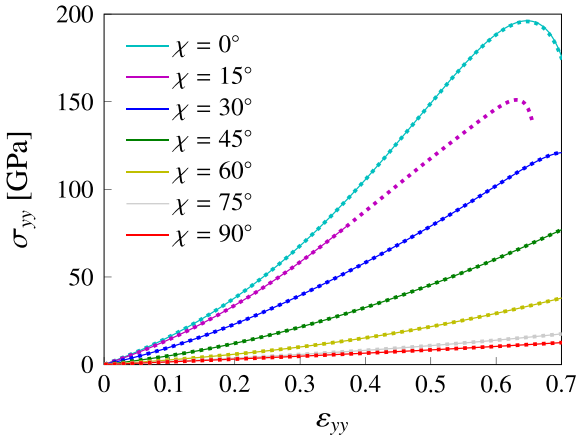

Fig. 9. Response of the transversely isotropic material for $\dot{\varepsilon}_{yy} = 10^{-4}/\,\mathrm{s}$ with the general nonlinear framework; solid lines - the arclength model, dotted lines - reference.

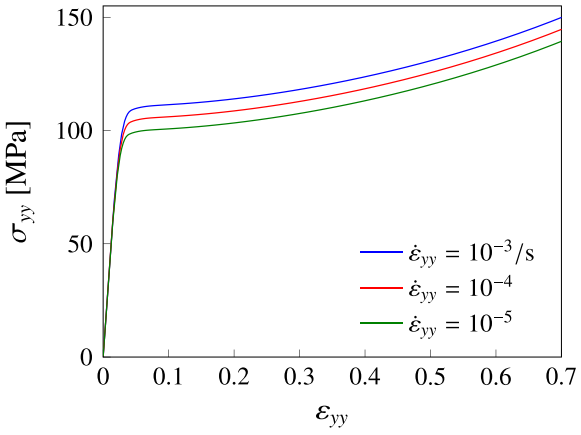

Fig. 10. The arclength model with the EGP material under different strain-rates.

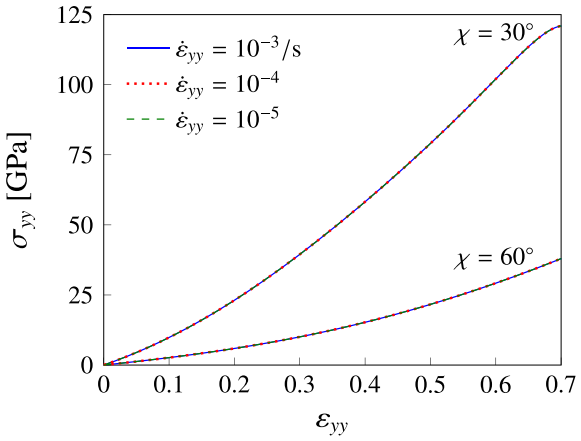

Fig. 11. The arclength model with the transversely isotropic material under different strain-rates.

ϕ. These simplifications lead to a large error when compared with the true stress–strain curve in moderate strain regime.

If in an intermediate formulation an update is made in $\hat{\mathbf{f}}$ for the deformation state of the RVE (shape "c" in Fig. 3), but there is no update in the orientation ($\phi = 0$), more accurate results are obtained, Fig. 6(right). For this isotropic material, the angle ϕ only becomes important around the strain level of 0.3, after which the response drifts away from the reference curve. This deviation is especially noticeable for the off-axis angles of 30°, 45° and 60°, when the shear stresses acting on the RVE increase. For 0° and 90°, there is no need to evaluate the angle ϕ because the edges of the micromodel do not rotate. Finally, if the model is updated according to the finite deformation framework including update of the angle ϕ, i.e. with Eqs. (27) and (34), it exactly matches the true stress–strain curve for all considered angles χ, Fig. 7.

The next example focuses on a homogeneous RVE with the hyperelastic transversely isotropic constitutive law (Bonet and Burton, 1998). Results obtained with the strain-rate based arclength model are compared with reference results. For off-axis loading of a homogeneous orthotropic material, a straightforward approach is available in which the load direction remains aligned with the global computational domain, while the preferential stiffness direction (i.e. the vector $\boldsymbol{A}$ in Fig. 5) is varied. According to this, reference results are generated from analysis of a simple cube, in which the vector $\boldsymbol{A}$ is varied with respect to the fixed loading direction. In the arclength model, this preferential stiffness direction always coincides with the local unit vector $\boldsymbol{e}_1$, see Fig. 2, while the orientation of the applied stress is varied. Again, three situations are examined, considering the strain-rate $\dot{\varepsilon}_{yy} = 10^{-4}/\,\mathrm{s}$. First, the small strain version of the arclength model produces inaccurate results when compared with the reference case, Fig. 8(left). This inaccuracy is most pronounced for the off-axis angles of 30° and 45°. Contrary to the isotropic EGP model, an update in $\hat{\mathbf{f}}$ for the past deformation process, but without a proper change in the orientation, does not lead to significant improvement of the results, Fig. 8(right). The off-axis angles of 0° and 90° are indeed exactly reproduced, since $\phi = 0$ in these cases, but the response for the other angles is markedly

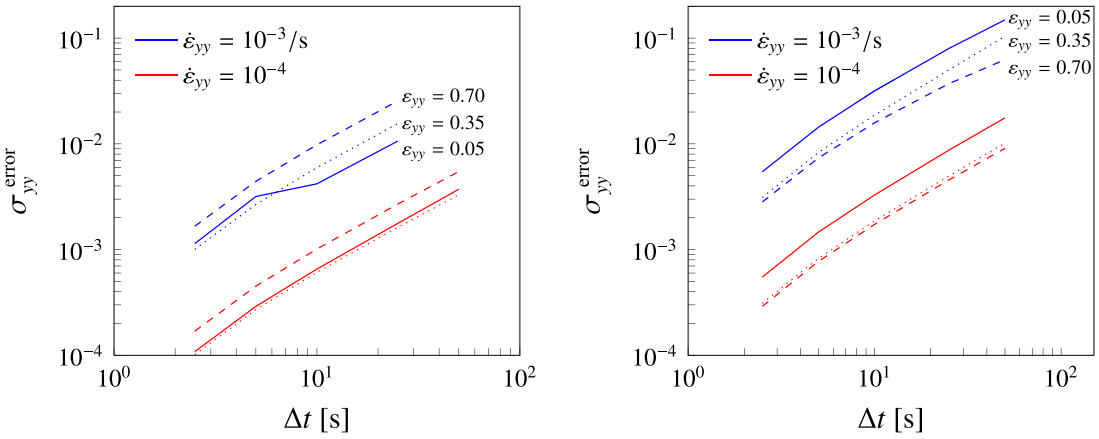

Fig. 12. Error in σ_{yy} for different time step sizes at different strain levels, measured relative to the case $\Delta t = 1$ s, for the EGP (left) and the transversely isotropic material (right).

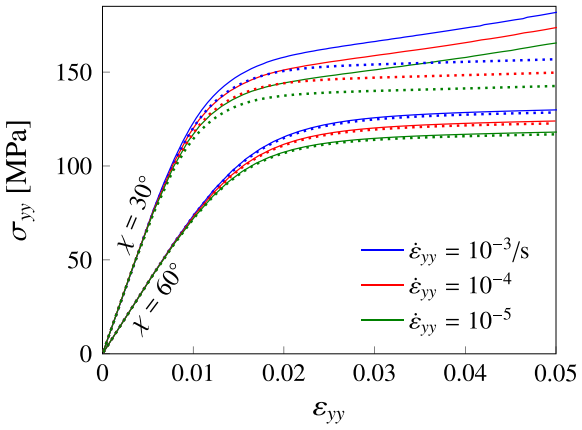

Fig. 13. The arclength model applied on thermoplastic composite RVE, considering different strain-rates and orientation of the fibers with respect to load direction; solid lines - general nonlinear framework, dotted lines - small strain version of the model.

incorrect. Finally, the adequately updated arclength model precisely matches the reference case, Fig. 9. From the same figure it is visible that the arclength model has not fully traced the equilibrium path of the reference case for $\chi = 15°$. The reason being a numerical instability in the Newton–Raphson iteration scheme. For all off-axis angles and all strain levels for which data were obtained, the results are in exact agreement with the reference results, even for very large strain values.

The following example deals with the rate-dependent aspects of the arclength model. The EGP is used as the material of the RVE, the off-axis angle is 45°,[5] and three different strain-rates are considered. The simulations have been done only with the general nonlinear framework. From Fig. 10 the conclusion arises that the arclength model is able to reproduce the rate-dependency of the material.

For completeness, rate dependency is also checked for the transversely isotropic material at two different off-axis angles. For this material there should be no influence of loading rate on the stress–strain response. In Fig. 11, the stress–strain curves obtained with three different loading rates in the general nonlinear framework are plotted. It can be observed that for both angles a unique rate-independent response is obtained. These results confirm that the rate-dependence found with the EGP material completely stems from the constitutive model.

[5] Since the material is isotropic, any other angle has the same relevance, except for 0° and 90° where some of the terms in the formulation remain 0.

It has been stated in the formulation part that some quantities of the model depend on the deformation state from the last converged time step. Namely, the unit force vector $\hat{\mathbf{f}}$ and the angle ϕ for time step n are determined from $\bar{\mathbf{F}}^{n-1}$. This choice leads to an error with respect to a fully implicit formulation, where the unit force vector and the constraint equation would be updated every iteration. This error will vanish upon reducing the time step size Δt. Therefore, it is important to check how the calculation step size Δt influences the accuracy of the output. An error is measured in the stress σ_{yy}, relative to the reference stress measured for $\Delta t = 1$ s. For this purpose Δt of: 2.5, 5, 10, 25 and 50 s has been chosen such that:

$$\sigma_{yy}^{\text{error}} = \left| \frac{\sigma_{yy}^{\text{ref}}(\Delta t = 1\text{s}) - \sigma_{yy}(\Delta t)}{\sigma_{yy}^{\text{ref}}(\Delta t = 1\text{s})} \right| \tag{63}$$

The error has been measured at strain levels of: 0.05, 0.35 and 0.7. The initial off-axis angle is 45°, since in this case the shear stresses acting on the RVE reach a maximum value, and the change in orientation is largest. Fig. 12(left) illustrates the error in a double logarithmic plot for the arclength model with the EGP material. The trend is such that the error increases with an increase in Δt. An increase in the strain-rate applied also increases the error, which is due to the fact that, at the same Δt, a higher strain-rate means larger strain increments. In the case of $\dot{\varepsilon}_{yy} = 10^{-3}$/s, it has not been possible to include a simulation with $\Delta t = 50$ s due to convergence problems. Common to both strain-rates is that the largest error is observed at the strain level of 0.7, and does not surpass 3%.

Fig. 12(right) shows the error for the transversely isotropic material. Here as well, the increase in the strain-rate enlarges the error, but this time it can exceed 10%. A conclusion drawn from the graphs is that at a strain-rate of 10^{-3}/s, a time step size of $\Delta t < 5$ s will keep the relative error below 1%. At higher strain-rates not considered in this study, it would be necessary to reduce Δt to a lower value.

The concluding example in this study is an RVE for an actual fiber reinforced composite material composed of thermoplastic polymer matrix (PEEK) and carbon fibers. The EGP material model represents the matrix part, whereas the transversely isotropic constitutive law with preferential stiffness direction parallel to the fiber axis is used for carbon fibers. The RVE is exposed to three different strain-rates, while considering two different orientations of the reinforcement with respect to the loading direction: $\chi = 30°$ and $\chi = 60°$. Results of the small strain version are compared with the stress–strain curves generated by applying the general nonlinear framework in Fig. 13. Both sets of results confirm that the strain-rate based arclength model can be used to simulate the response of UD composite systems on the microlevel, accounting for off-axis loading and an arbitrary strain-rate. Whereas the difference between the small strain and the finite strain version of the model is negligible for $\chi = 60°$, it increases for lower off-axis angles.

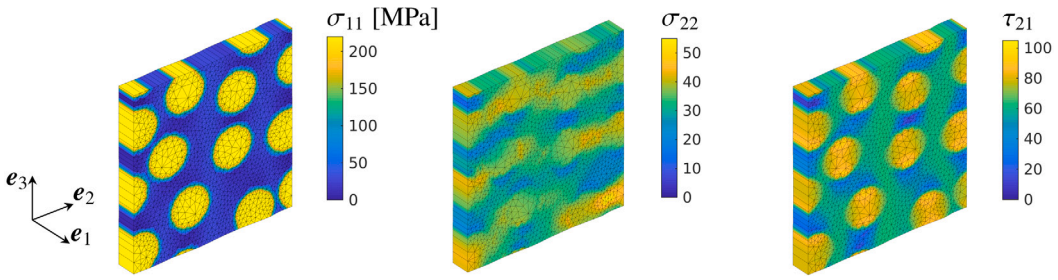

Fig. 14. Stress distribution in local coordinate system of the RVE, for $\chi = 30°$ and $\dot{\varepsilon}_{yy} = 10^{-4}$/ s, at $\varepsilon_{yy} = 0.025$; finite element mesh is generated with Gmsh (Geuzaine and Remacle, 2009).

The reason for this change in the difference is that in the range of low off-axis angles, a small variation in this angle significantly changes the axial stress component in the stiff carbon fibers. This variation in the off-axis angle is zero in the case of the small strain version model, and the hardening effect due to the change in orientation is not captured.

The contour plots of Fig. 14 show the distribution of the three stress components in the local frame of the RVE analyzed with the general nonlinear framework. While σ_{22} and τ_{21} components are distributed between the matrix and fibers, the σ_{11} component is almost exclusively taken by the fibers.

6. Conclusion

In this paper a strain-rate based arclength model that enables geometric and material nonlinear analysis of unidirectional composite systems at the microlevel is introduced. The same RVE can be used to simulate response of a UD composite material subjected to an arbitrary strain-rate, with an arbitrary orientation of the reinforcement relative to the loading direction. The constraint equation of the model ensures that the deformation pattern of the RVE corresponds to the strain-rate in the global loading direction, imposed in the analysis. Moreover, in order to ensure that the local stress state remains consistent with global uniaxial stress even when the RVE deforms and rotates, the unit force vector of the arclength model is updated as a function of the deformation state. A simplification is made that the change in orientation of the RVE and the unit force vector depend on the converged deformation state from the last time step. The numerical analysis has shown that the error induced by this explicit approach can be kept below 1% by properly choosing the size of the time increment. Several examples have been considered in order to show that the model accounts for different off-axis angles, captures finite strains exactly, and resolves the rate-dependency of the material. The intended usage of the method has been demonstrated with the simulation of the rate-dependent response of fiber-reinforced thermoplastic composite material resulting in homogenized stress–strain curves and microscopic stress distributions.

A small strain version of the model has been derived from the general nonlinear framework. In the case of the composite RVE, it has been shown that this version of the model gives results that differ significantly from those obtained with the general nonlinear framework, particularly for lower off-axis angles. For the homogeneous transversely isotropic material this difference is most pronounced for off-axis angles in the range 30°–45°.

The arclength model has been derived without any assumptions on the constitutive behavior. Therefore the framework can also be used to investigate the failure of composite materials under off-axis loading when softening behavior and/or cohesive cracking is included in the micromodel formulation.

Declaration of competing interest

The authors declare that they have no known competing financial interests or personal relationships that could have appeared to influence the work reported in this paper.

Data availability

Data presented in this article are available at the 4TU.ResearchData repository through https://doi.org/10.4121/17166974.v1.

Acknowledgments

This research forms part of the research programme of DPI, The Netherlands, project #811t17.

Appendix. Periodic boundary conditions

The periodicity in the RVE geometry enables application of periodic boundary conditions. Linear constraints are imposed between corresponding degrees of freedom on opposite faces of the RVE. For this purpose, four master nodes are defined at corners of the RVE, see Fig. 2. Let x_i represent coordinates in local coordinate frame, where $i = 1, 2, 3$. The relative displacement between matching nodes on opposite sides of the RVE is equal to the difference in displacement between corresponding master nodes:

$$\begin{aligned}
\mathbf{u}(l_1^0, x_2, x_3) &= \mathbf{u}(0, x_2, x_3) + \mathbf{u}(l_1^0, 0, 0) - \mathbf{u}(0, 0, 0) \\
\mathbf{u}(x_1, l_2^0, x_3) &= \mathbf{u}(x_1, 0, x_3) + \mathbf{u}(0, l_2^0, 0) - \mathbf{u}(0, 0, 0) \\
\mathbf{u}(x_1, x_2, l_3^0) &= \mathbf{u}(x_1, x_2, 0) + \mathbf{u}(0, 0, l_3^0) - \mathbf{u}(0, 0, 0)
\end{aligned} \tag{A.1}$$

where l_i^0 is the initial length of the RVE in direction i, $\mathbf{u}(l_1^0, 0, 0)$, $\mathbf{u}(0, l_2^0, 0)$ and $\mathbf{u}(0, 0, l_3^0)$ are displacements on master nodes 1, 2 and 3, respectively, whereas $\mathbf{u}(0, 0, 0)$ represent displacements on master node 0. Any added displacement constraint is automatically substituted in all existing displacement constraints, such that a single degree of freedom cannot be a slave and a master node simultaneously. As part of the arclength control method, a unit force vector is specified on the master nodes, see Fig. 2. The magnitude of every unit force component, multiplied with the load factor λ of the arclength method, is distributed among the nodes belonging to the RVE face on which the force component is acting when the constraints are applied.

References

Arteiro, A., Catalanotti, G., Melro, A.R., Linde, P., Camanho, P.P., 2014. Micro-mechanical analysis of the in situ effect in polymer composite laminates. Compos. Struct. 116, 827–840. http://dx.doi.org/10.1016/j.compstruct.2014.06.014.

Belytschko, T., Liu, W.K., Moran, B., Elkhodary, K., 2014. Nonlinear Finite Elements for Continua and Structures. John Wiley & Sons.

Bonet, J., Burton, A.J., 1998. A simple orthotropic, transversely isotropic hyperelastic constitutive equation for large strain computations. Comput. Methods Appl. Mech. Engrg. 162 (1), 151–164. http://dx.doi.org/10.1016/S0045-7825(97)00339-3.

Crisfield, M.A., 1982. Accelerated solution techniques and concrete cracking. Comput. Methods Appl. Mech. Engrg. 33 (1), 585–607. http://dx.doi.org/10.1016/0045-7825(82)90124-4.

De Borst, R., 1987. Computation of post-bifurcation and post-failure behavior of strain-softening solids. Comput. Struct. 25 (2), 211–224. http://dx.doi.org/10.1016/0045-7949(87)90144-1.

De Borst, R., Crisfield, M.A., Remmers, J.J.C., Verhoosel, C.V., 2012. Nonlinear Finite Element Analysis of Solids and Structures. John Wiley & Sons.

Eyring, H., 1936. Viscosity, plasticity, and diffusion as examples of absolute reaction rates. J. Chem. Phys. 4 (4), 283–291. http://dx.doi.org/10.1063/1.1749836.

Geuzaine, C., Remacle, J.-F., 2009. Gmsh: A 3-D finite element mesh generator with built-in pre- and post-processing facilities. Internat. J. Numer. Methods Engrg. 79 (11), 1309–1331. http://dx.doi.org/10.1002/nme.2579.

Govaert, L.E., Schellens, H.J., Thomassen, H.J.M., Smit, R.J.M., Terzoli, L., Peijs, T., 2001. A micromechanical approach to time-dependent failure in off-axis loaded polymer composites. Composites A 32 (12), 1697–1711. http://dx.doi.org/10.1016/S1359-835X(01)00028-8.

Gutiérrez, M.A., 2004. Energy release control for numerical simulations of failure in quasi-brittle solids. Commun. Numer. Methods. Eng. 20 (1), 19–29. http://dx.doi.org/10.1002/cnm.649.

Klompen, E.T.J., Engels, T.A.P., Govaert, L.E., Meijer, H.E.H., 2005. Modeling of the postyield response of glassy polymers: Influence of thermomechanical history. Macromolecules 38 (16), 6997–7008. http://dx.doi.org/10.1021/ma050498.v.

Klompen, E., Govaert, L., 1999. Nonlinear viscoelastic behaviour of thermorheologically complex materials. Mech. Time Depend. Mater. 3 (1), 49–69. http://dx.doi.org/10.1023/A:1009853024441.

Van der Meer, F.P., 2016. Micromechanical validation of a mesomodel for plasticity in composites. Eur. J. Mech. A Solids 60, 58–69. http://dx.doi.org/10.1016/j.euromechsol.2016.06.008.

Van der Meer, F.P., Oliver, C., Sluys, L.J., 2010. Computational analysis of progressive failure in a notched laminate including shear nonlinearity and fiber failure. Compos. Sci. Technol. 70 (4), 692–700. http://dx.doi.org/10.1016/j.compscitech.2010.01.003.

Melro, A.R., Camanho, P.P., Pinho, S.T., 2012. Influence of geometrical parameters on the elastic response of unidirectional composite materials. Compos. Struct. 94 (11), 3223–3231. http://dx.doi.org/10.1016/j.compstruct.2012.05.004.

Naya, F., González, C., Lopes, C.S., Van der Veen, S., Pons, F., 2017. Computational micromechanics of the transverse and shear behavior of unidirectional fiber reinforced polymers including environmental effects. Composites A 92, 146–157. http://dx.doi.org/10.1016/j.compositesa.2016.06.018.

Ramm, E., 1981. Strategies for tracing the nonlinear response near limit points. In: Wunderlich, W., Stein, E., Bathe, K.-J. (Eds.), Nonlinear Finite Element Analysis in Structural Mechanics. Springer, Berlin, Heidelberg, pp. 63–89. http://dx.doi.org/10.1007/978-3-642-81589-8_5.

Riks, E., 1972. The application of Newton's method to the problem of elastic stability. J. Appl. Mech. 39 (4), 1060–1065. http://dx.doi.org/10.1115/1.3422829.

Rocha, I.B.C.M., Van der Meer, F.P., Nijssen, R.P.L., Sluys, L.J., 2017. A multiscale and multiphysics numerical framework for modelling of hygrothermal ageing in laminated composites. Internat. J. Numer. Methods Engrg. 112 (4), 360–379. http://dx.doi.org/10.1002/nme.5542.

Senden, D.J.A., Krop, S., van Dommelen, J.A.W., Govaert, L.E., 2012. Rate- and temperature-dependent strain hardening of polycarbonate. J. Polym. Sci. B 50 (24), 1680–1693. http://dx.doi.org/10.1002/polb.23165.

Totry, E., González, C., Llorca, J., 2008. Failure locus of fiber-reinforced composites under transverse compression and out-of-plane shear. Compos. Sci. Technol. 68 (3), 829–839. http://dx.doi.org/10.1016/j.compscitech.2007.08.023.

Van Breemen, L.C.A., Klompen, E.T.J., Govaert, L.E., Meijer, H.E.H., 2011. Extending the EGP constitutive model for polymer glasses to multiple relaxation times. J. Mech. Phys. Solids 59 (10), 2191–2207. http://dx.doi.org/10.1016/j.jmps.2011.05.001.

Verhoosel, C.V., Remmers, J.J.C., Gutiérrez, M.A., 2009. A dissipation-based arc-length method for robust simulation of brittle and ductile failure. Internat. J. Numer. Methods Engrg. 77 (9), 1290–1321. http://dx.doi.org/10.1002/nme.2447.

Wempner, G.A., 1971. Discrete approximations related to nonlinear theories of solids. Int. J. Solids Struct. 7 (11), 1581–1599. http://dx.doi.org/10.1016/0020-7683(71)90038-2.